The Astrophysical Journal, 836:100 (9pp), 2017 February 10 https://doi.org/10.3847/1538-4357/836/1/100

The Re-Acceleration of Galactic Electrons at the Heliospheric Termination Shock

P. L. Prinsloo, M. S. Potgieter, and R. D. Strauss
Centre for Space Research, North-West University, 2520 Potchefstroom, South Africa; marius.potgieter@nwu.ac.za
Received 2016 September 30; revised 2016 November 17; accepted 2016 November 25; published 2017 February 10

Abstract

Observations by the *Voyager* spacecraft in the outer heliosphere presented several challenges for the paradigm of diffusive shock acceleration (DSA) at the solar wind termination shock (TS). In this study, the viability of DSA as a re-acceleration mechanism for galactic electrons is investigated using a comprehensive cosmic-ray modulation model. The results demonstrate that the efficiency of DSA depends strongly on the shape of the electron spectra incident at the TS, which in turn depends on the features of the local interstellar spectrum. Modulation processes such as drifts therefore also influence the re-acceleration process. It is found that re-accelerated electrons make appreciable contributions to intensities in the heliosphere and that increases caused by DSA at the TS are comparable to intensity enhancements observed by *Voyager* 1 ahead of the TS crossing. The modeling results are interpreted as support for DSA as a re-acceleration mechanism for galactic electrons at the TS.

Key words: acceleration of particles – cosmic rays – solar wind – Sun: heliosphere

1. Introduction

The *Voyager* 1 and 2 spacecraft, respectively, crossed the solar wind (SW) termination shock (TS) of the heliosphere at radial distances of 94 and 84 au from the Sun (Stone et al. 2005; Burlaga et al. 2008). Prior to the TS crossing of *Voyager* 1, two distinct enhancements of 6–14 MeV electrons were observed, each lasting for several months (McDonald et al. 2003; Stone et al. 2005, 2008). The intensities at the highest point of these enhancements were higher than the background intensity by a factor of at least 2.5. These particle events were thought to be indicative of the re-acceleration of galactic electrons at the TS, with most interpretations hinging on the involvement of diffusive shock acceleration (DSA; see, e.g., Axford et al. 1977). They were interpreted as precursors to the TS crossing and likely arose as a result of the streaming of accelerated particles along temporary magnetic connections between the TS and the spacecraft (see Giacalone & Jokipii 2006, and the references therein).

DSA has since come under increased criticism when it was discovered that the acceleration region of anomalous cosmic rays (ACRs) was not at the TS along *Voyager* 1's trajectory (Decker et al. 2005; Stone et al. 2005). The long-held paradigm of ACRs being formed by the DSA of pick-up ions at the TS (Fisk et al. 1974; Pesses et al. 1981) came under scrutiny, and interest subsequently shifted to alternative acceleration mechanisms; see Giacalone et al. (2012) for a review of these mechanisms. Some authors (e.g., Jokipii et al. 2007; Schwadron et al. 2008) maintain, however, that DSA remains a viable mechanism for ACR acceleration, while the power-law distributions of TS particles observed below 3 MeV nuc^{-1} (Stone et al. 2005) are also considered to follow from DSA; see the related discussion by Lee et al. (2009). Although the involvement of DSA was furthermore questioned in the acceleration of very-low-energy ions (Fisk et al. 2006), there has not been a formal investigation into its viability as a local re-acceleration mechanism for galactic electrons.

From a modulation perspective, interesting revelations with regards to galactic electrons have recently been made. With the crossing of the heliopause (HP) by *Voyager* 1 (Gurnett et al. 2013; Webber & McDonald 2013) it was revealed that the very local interstellar spectrum of these electrons is power-law distributed at energies of 6–60 MeV (Stone et al. 2013; Cummings et al. 2016). The observation of this power-law form in the inner heliosheath prior to the HP crossing was interpreted as a feature of rigidity-independent modulation (Potgieter 1996; Caballero-Lopez et al. 2010; Potgieter & Nndanganeni 2013), while the large intensity gradient observed across the heliosheath (Webber et al. 2012) is indicative of efficient particle scattering in this region. These insights allow improved modeling of the features of electron energy spectra at the TS. Revisiting the re-acceleration of galactic electrons at the TS is considered appropriate, not only in an attempt to gain general insight into the particle events observed by *Voyager* 1 near the TS, but also to determine what may reasonably be expected from DSA now that the features of electron spectra in the outer heliosphere have been explored. This is done within the context of the results of a galactic cosmic-ray (CR) modulation model. Direct comparison with observations will be presented in a follow-up report.

2. A Re-Acceleration Model for Electron Modulation

The transport of galactic electrons in the heliosphere is described using the classical Parker (1965) transport equation (TPE), given by

$$\frac{\partial f}{\partial t} = -(\boldsymbol{V}_{\rm sw} + \langle \boldsymbol{v}_D \rangle) \cdot \nabla f + \nabla \cdot (\boldsymbol{K}_s \cdot \nabla f) + \tfrac{1}{3}(\nabla \cdot \boldsymbol{V}_{\rm sw}) \partial f / \partial \ln P, \quad (1)$$

for an isotropic distribution function $f = f(r, \theta, P, t)$, which is related to the differential intensity $j = P^2 f$, with P, r, θ, and t each denoting rigidity, radial distance, colatitude (polar angle), and time. The terms from left to right in Equation (1) describe time-dependent changes, convection caused by the SW flow at a velocity of $\boldsymbol{V}_{\rm sw}$, CR drifts in terms of the pitch-angle averaged drift velocity $\langle \boldsymbol{v}_D \rangle$, spatial diffusion as described by the diffusion tensor $\boldsymbol{K}_s$, and adiabatic energy changes through the divergence of the SW velocity.

The TPE is solved numerically using a two-dimensional (2D) drift-DSA model originally developed by le Roux et al.

(1996) and later modified by Langner et al. (2004). Variants of this same model were successfully implemented in studying the modulation and acceleration of various species of CRs (e.g., Ferreira et al. 2004; Langner et al. 2006a, 2006b; Strauss et al. 2010; Ngobeni & Potgieter 2015). The model is iterated several times until sufficient convergence of the numerical solution is attained, while transport coefficients are kept time-independent. The finite-difference numerical scheme is not unconditionally stable for more than three computational dimensions so that our model is restricted to time, energy, and two spatial dimensions. This implies an azimuthally symmetric heliosphere, which is reasonable considering that electron modulation differs marginally if this dimension is included, both in general (Ferreira et al. 1999) and in the nose-heliosheath (Ferreira & Scherer 2004).

All solutions are shown along the approximate line of travel of *Voyager* 1 at a polar angle of $\theta = 55^\circ$ and for solar-quiet conditions with the heliospheric current sheet (HCS) tilt angle specified as $\alpha = 10^\circ$. The local interstellar spectrum for electrons, the configurations of drifts and the diffusion coefficients, and the TS compression ratio are all kept unchanged; see Ferreira & Potgieter (2002) and Ferreira et al. (2004) for studies on the effects of varying these properties. These and other pertinent model details are discussed under the headings below.

2.1. Heliospheric Properties

This study focuses on the near-equatorial nose region of the heliosphere explored by the *Voyager* spacecraft, and with this region in mind the heliosphere is approximated as being spherical with symmetries about the polar and equatorial planes. The positions of the TS and the HP are specified as $r_{\rm TS} = 94$ au and $r_{\rm HP} = 122$ au to reflect the *Voyager* 1 detections of these boundaries. Because CR modulation beyond the HP is small (Strauss et al. 2013; Luo et al. 2016), $r_{\rm HP}$ is assumed as the outer modulation boundary.

The SW flow is assumed to be radial out to the TS with a bulk speed of 400 km s^{-1} in the equatorial regions, but transitioning up to 800 km s^{-1} in the polar regions during solar minimum conditions (see also Moeketsi et al. 2005; Potgieter et al. 2014). At the TS, this radial speed decreases abruptly by the compression ratio s. Following le Roux et al. (1996) and Langner et al. (2004), this decrease is modeled according to

$$V_{\rm sw} = \frac{V}{2s}\left[(s+1) - (s-1)\tanh\left(\frac{r - r_{\rm TS}}{L}\right)\right] \qquad (2)$$

for $r < r_{\rm TS}$, with $V_{\rm sw} = V_{\rm sw}(r, \theta)$, and where $V = V_{\rm sw}(r_{\rm TS} - L, \theta)$ is the upstream SW speed. The length of $L = 1.2$ au stipulates the extent across which the radial SW speed decreases with a factor of $s/2$ before decreasing discontinuously with another $s/2$ factor at $r_{\rm TS}$. This length scale does not necessarily represent the physical TS ramp width, but is chosen to reproduce, using Equation (2), the decrease of the SW speed across the TS region as observed by *Voyager* 2. See Luo et al. (2013) for the effect of varying this shock width on the re-acceleration of protons. A value of $s = 2.5$ is used in this paper as an average value of those estimated from *Voyager* 1 CR data (Stone et al. 2005), from *Voyager* 2 plasma measurements (Richardson et al. 2008), and magnetometer data from both spacecraft (Burlaga et al. 2005, 2008). The SW compression at the TS causes a negative divergence of the SW velocity, which translates to particle acceleration in the TPE (e.g., Jokipii 1987). Further upstream, this divergence is assumed positive, which allows adiabatic cooling of CRs. Downstream, the SW speed is specified to decrease as $1/r^2$ which implies incompressibility. This ensures that the only particle acceleration in the model takes place as a result of DSA at the TS. For alternative SW speed scenarios in the heliosheath and their consequences, see Langner et al. (2006a, 2006b) and Strauss et al. (2010). The HMF geometry is described according to the Parker (1958) model but modified in the polar regions as proposed by Jokipii & Kóta (1989).

2.2. Transport Coefficients

The pitch-angle averaged drift velocity resulting from the curvature, gradient, and polarity changes of the HMF is given by $\boldsymbol{v}_{D,gc} = \nabla \times \kappa_D \hat{\boldsymbol{e}}_B$, where $\hat{\boldsymbol{e}}_B$ is a unit vector directed along the average HMF direction. The drift coefficient κ_D is expressed for a general case as

$$\kappa_D = \frac{v}{3} r_L \frac{(\omega\tau_d)^2}{1 + (\omega\tau_d)^2}, \qquad (3)$$

where $(\omega\tau_d)^2/(1 + (\omega\tau_d)^2)$, with ω the particle's gyro-frequency and τ_d a scattering timescale determined by turbulence, is used to reduce drifts (e.g., Engelbrecht & Burger 2015; Ngobeni & Potgieter 2015). In the weak-scattering limit ($\omega\tau_d \gg 1$), κ_D scales as the Larmor radius $r_{\rm L} = P/Bc$, where B is the HMF magnitude and c is the speed of light (Potgieter & Moraal 1985). Following Burger et al. (2000), it is approximated that $\omega\tau_d \sim P$, which causes a reduction of κ_D from its weak-scattering value at low rigidities. Drifts along the HCS are described using an azimuthally averaged current sheet model developed by Langner & Potgieter (2005).

The symmetrical diffusion tensor $\boldsymbol{K}_s$ in HMF-aligned coordinates has diagonal elements of $\kappa_{\parallel}$, $\kappa_{\perp r}$, and $\kappa_{\perp\theta}$, which, respectively, describe the spatial diffusion of CRs parallel to the mean HMF direction and perpendicular to it in the radial and polar directions. These diffusion coefficients are related to the particle's mean-free path λ (MFP) according to $\kappa = (v/3)\lambda$, where v is the particle's speed. The rigidity dependence of $\lambda_{\parallel}$ follows that employed by Potgieter et al. (2015), which in turn is based on reproductions of electron observations and approximates the basic form of $\lambda_{\parallel}$ predicted by turbulence theory (Teufel & Schlickeiser 2003). According to this simplified configuration, $\lambda_{\parallel}$ is specified to be rigidity-independent up to ~0.4 GV, from where it increases as $\sim P^{1.2}$ at higher rigidities. The effective radial dependence is $\lambda_{\parallel} \sim \lambda_0 (r/r_0)$ at $r \leqslant r_{\rm TS}$, where $\lambda_0 \approx 0.4$ au is the MFP value at the Earth ($r = r_0$). At $r > r_{\rm TS}$, the large modulation in the heliosheath is simulated with small MFP values. It is assumed that $\lambda_{\parallel} \sim \lambda_r(r_{\rm TS^+})(r/r_{\rm TS})^2$ in the heliosheath, where $\lambda_r(r_{\rm TS^+})$ is the downstream MFP value at the TS. For $\kappa_{\perp r/\theta}$, the perpendicular diffusion coefficients of Burger et al. (2000) are used, though they are modified for electrons to retain the rigidity dependence of $\kappa_{\parallel}$. These coefficients are configured such that $\kappa_{\perp\theta} = \kappa_{\perp r}$ near the equatorial regions, but with polar diffusion enhanced at larger colatitudes so that diffusion becomes increasingly anisotropic ($\kappa_{\perp\theta} > \kappa_{\perp r}$) toward the poles (see also Ngobeni & Potgieter 2015). This enhancement of $\kappa_{\perp\theta}$

was initially introduced to reproduce the small latitudinal gradients observed by the Ulysses spacecraft and to counteract very large drifts in the polar regions; see Heber & Potgieter (2006) and also the motivations provided by Potgieter (1996), Burger et al. (2000), and Ferreira et al. (2000).

2.3. The Heliopause Spectrum

The modulation of galactic electrons is considered to begin at the HP, where an unmodulated spectrum is specified as an initial condition for electron modulation. Following Potgieter et al. (2015), this heliopause spectrum (HPS), or very local interstellar spectrum, is modeled to resemble two power laws at energies exceeding ∼4 MeV and expressed as

$$j_{\rm HPS} = \frac{0.16}{\beta^2}\left(\frac{E}{E_N}\right)^{h_1}\left(\frac{(E)^{h_t}+(E_b)^{h_t}}{(E_N)^{h_t}+(E_b)^{h_t}}\right)^{(h_2-h_1)/h_t} \quad (4)$$

in units of electrons $\rm m^{-2}\ s^{-1}\ sr^{-1}\ MeV^{-1}$, with $\beta = v/c$ the ratio of particle to light speed and $E_N = 1$ GeV. $E_b = 0.67$ GeV denotes the energy about which the transition between power laws occurs and $h_t = 1.5$ determines its smoothness. The quantities h_1 and h_2 refer to the power-law indices at energies, respectively, below and above E_b. Two values are considered for h_1, namely -1.55 and -1.35, which are, respectively, informed by the lower and upper limits on the spectral index observed by *Voyager* 1 at energies of 6–60 MeV (Stone et al. 2013). Toward higher energies modulation progressively phases out because of increasingly larger MFPs and becomes negligible above ∼30 GeV (Strauss & Potgieter 2014), allowing for the inference of the HPS from observations at Earth. The value of h_2 is thus taken as -3.18 to reflect the index observed by PAMELA above ∼5 GeV (Menn et al. 2013; Adriani et al. 2015). Similar HPS features are also obtained by Bisschoff & Potgieter (2014) using galactic propagation modeling. See also the discussions by Potgieter et al. (2015) and Potgieter (2014b).

3. A Short Recapitulation of Diffusive Shock Acceleration

The effects of DSA at the TS is implicitly accounted for in the TPE of Equation (1) through the term describing adiabatic energy changes, which becomes very large and negative in the TS region, and causes net acceleration of particles (e.g., Jokipii 1982, 1986, 1987). An energy spectrum resulting from the DSA of a mono-energetic source of CRs for the one-dimensional scenario is known to resemble a power law with a spectral index that is a function only of the compression ratio of the involved shock; see, e.g., the description by Potgieter & Moraal (1988). The shock-accelerated distribution function thus has the form $f(P) \propto P^{-3/(s-1)}$, implying a differential intensity of $j(P) \propto P^{(s+2)/(1-s)}$, which as a function of kinetic energy is given as

$$j(E) \propto E^{\gamma(s)}, \quad (5)$$

where it follows that

$$\gamma(s) = \frac{s+2}{1-s}, \quad (6)$$

for $E \gg E_0$. This power-law form subsides at the energy for which the diffusion length scales of particles at the TS become comparable to $r_{\rm TS}$ for the 2D scenario (see also Steenberg & Moraal 1999). At this energy, particles escape the TS region and an exponential decrease of intensities ensues.

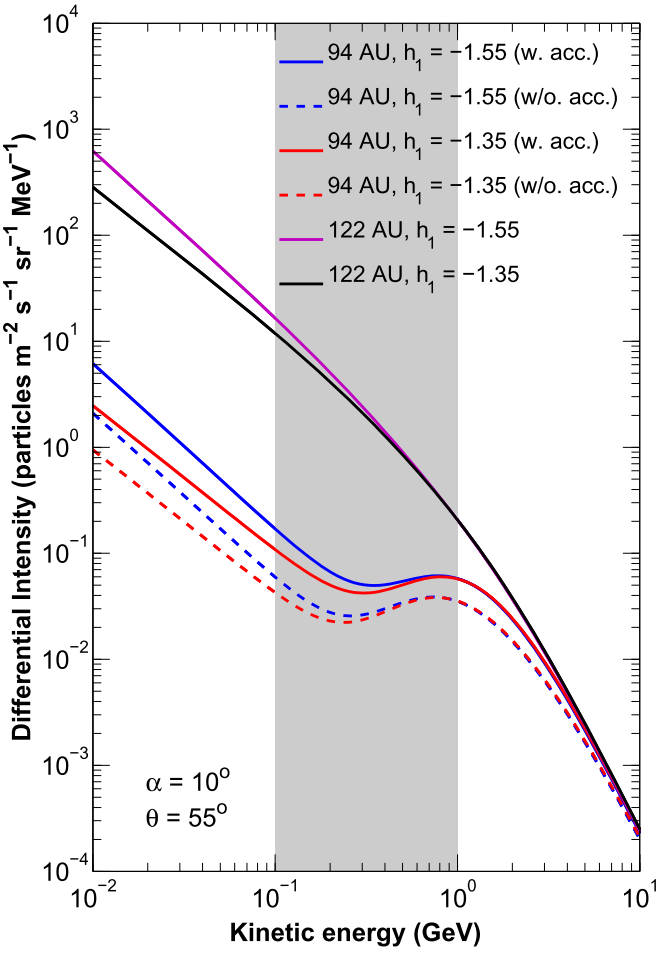

Figure 1. Modeled electron energy spectra for two configurations of the HPS. The TS spectra at 94 au shown in red and blue are, respectively, modulated from the HPS at 122 au with $h_1 = -1.35$ (in black) and -1.55 (in magenta) in Equation (4). Solid and dashed lines, respectively, represent TS spectra with and without acceleration. The shaded and unshaded bands indicate three distinct energy regions classified in Section 4.1. These solutions are shown at a colatitude of $\theta = 55°$ and for solar minimum conditions, $\alpha = 10°$. Drifts are neglected for these solutions.

The spectrum of galactic electrons at the TS is of course not a mono-energetic source, but bears features of prior acceleration, propagation and energy changes in galactic space, and modulation within the heliosphere. Denoting the initial spectral indices of energy spectra incident at the TS as $\chi(E)$ and their indices after acceleration as $\gamma^*(E)$, two general cases are considered for the re-acceleration of electron spectra at the TS. First, should the spectral indices of the incident TS spectrum be smaller than the DSA-associated index given by Equation (6), the re-accelerated spectrum adopts the latter index. That is, for

$$\chi(E) < \gamma(s), \quad (7)$$

it follows that

$$\gamma^*(E) \approx \gamma(s). \quad (8)$$

The initial spectrum is hence hardened to reflect the shock-accelerated spectrum associated with the TS compression ratio. However, if incident spectra exhibit spectral indices exceeding the index given by Equation (6), their spectral indices are not

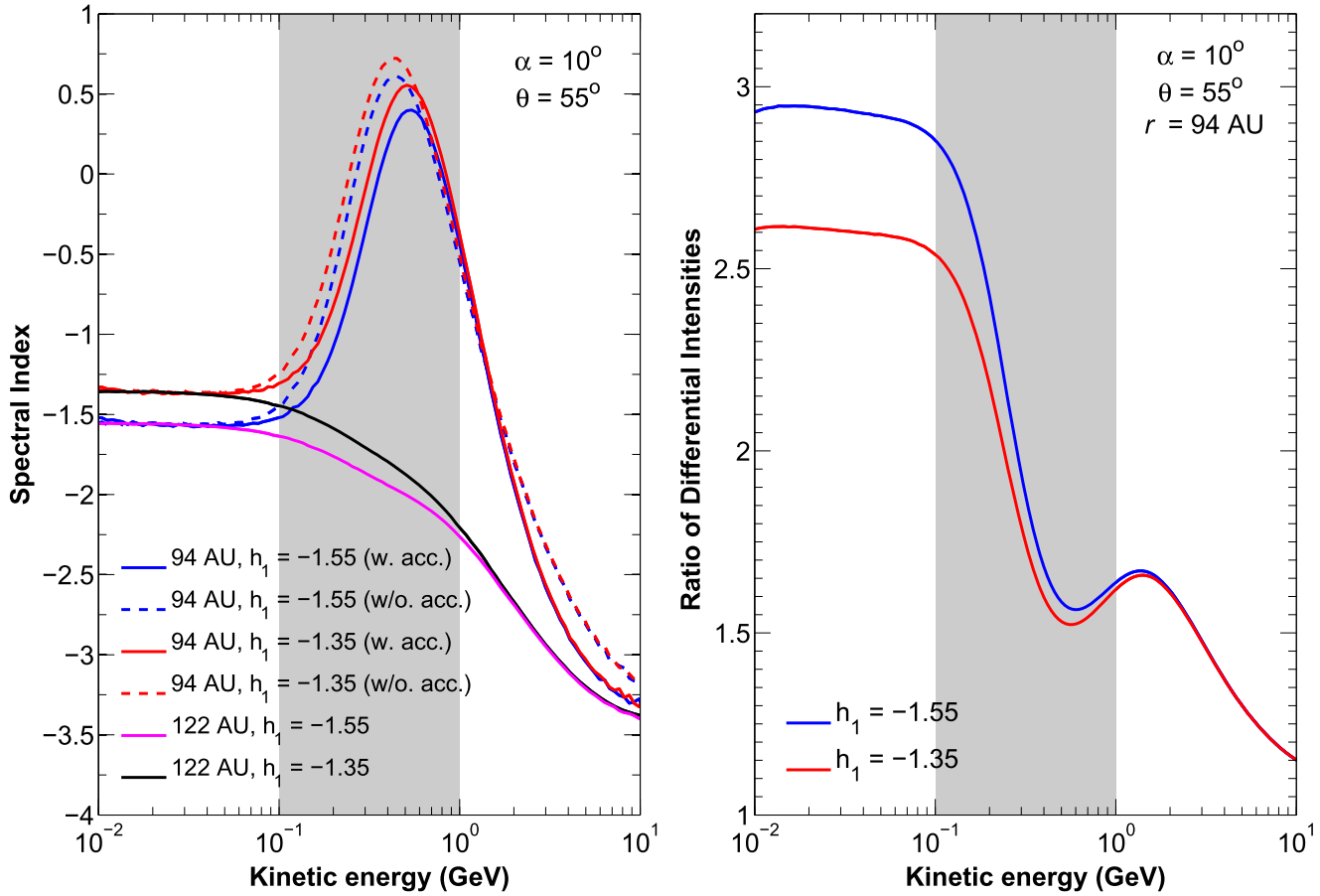

Figure 2. Left: the spectral indices of the energy spectra presented in Figure 1 with the lines representing the same configurations as defined in that figure. Right: ratios of the TS spectra presented in Figure 1 with acceleration to those without, indicative of what factor re-acceleration is contributing to intensities. The blue and red lines, respectively, represent the aforementioned ratios corresponding to HPS configurations with $h_1 = -1.55$ and -1.35 in Equation (4). The shaded and unshaded bands are as explained for Figure 1.

expected to change as significantly as a result of DSA. Hence, for

$$\chi(E) > \gamma(s), \tag{9}$$

it follows that

$$\gamma^*(E) \approx \chi(E - \epsilon). \tag{10}$$

In this case, the spectrum is shifted to higher energies by some amount denoted ϵ and has its intensities raised during re-acceleration. See related discussions by Axford (1981) and Jones & Ellison (1991) for a comprehensive review.

Section 4 evaluates the properties of the energy spectra of galactic electrons incident at the TS at the hand of the conditions given in Equations (7) and (9) and discusses the resulting effects of re-acceleration.

4. Spectral Features of Electron Re-acceleration

The conditions stipulated in Equations (7)–(10) provide guidelines to how electron energy spectra at the TS are altered by DSA and show that it is dependent on the shape of the incident spectrum. While taking into account how modulation processes alter the shape of these TS spectra, the extent to which DSA is expected to re-accelerate galactic electrons at different energies is subsequently investigated, with interesting results.

4.1. Dependence of Re-acceleration on the Form of Termination Shock Spectra

If the spectrum incident at the TS retains the exact form of the HPS, as given by Equation (4), no significant hardening of this spectrum is expected as a result of DSA. This is because the HPS is generally harder than the spectra produced through DSA at a TS with $s = 2.5$, which is unable to yield a spectral index that is larger than -3 for relativistic electrons according to Equation (6). In this case, the condition of Equation (9) applies. The TS spectrum is, however, a modulated form of the HPS with its features depending on the rigidity dependence of the diffusion coefficients. Figure 1 shows modeled TS spectra as modulated from two configurations of the HPS with $h_1 = -1.55$ and -1.35 respectively. Three regions with distinct spectral characteristics can be classified: In the first region, extending up to 0.1 GeV, TS spectra retain the power-law form of the HPS as a result of the rigidity-independence of the diffusion coefficients at those energies. In the second energy region (0.1–1 GeV) the power law at low energies flattens out as the diffusion coefficients grow with increasing rigidity. For convenience, this region is referred to as the transition region. The third region extends from 1 GeV to higher energies with modulation progressively phasing out.

What primarily distinguishes these three energy regions are the values of the spectral indices in each. These values are plotted in the left-hand side of Figure 2 as a function of kinetic

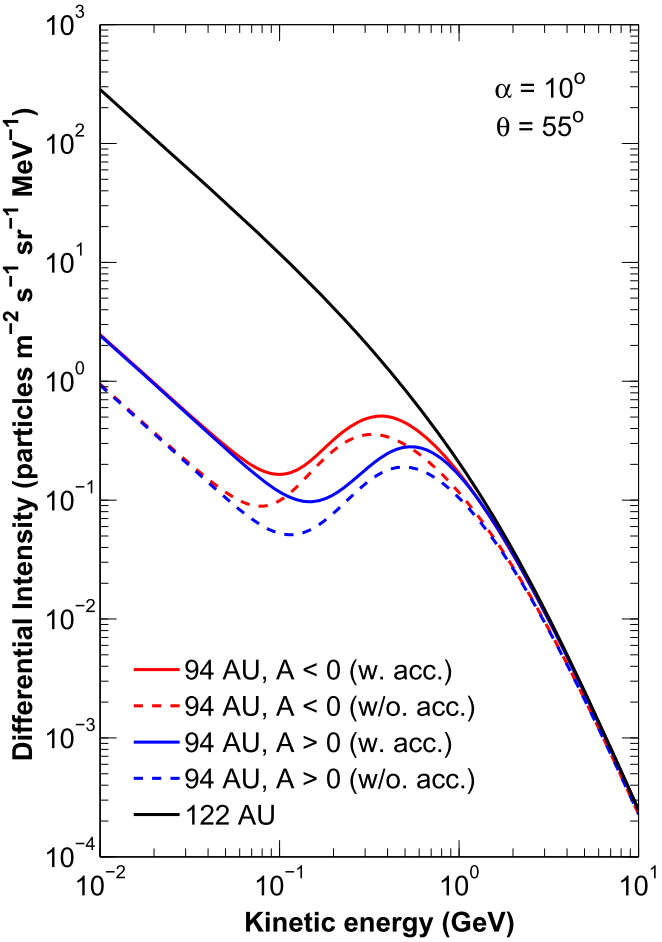

Figure 3. Modeled electron spectra illustrating the effects of drifts for the two solar magnetic polarities; TS spectra at 94 au for the $A < 0$ and $A > 0$ cycles are shown in red and blue, respectively, with acceleration (solid lines) and without acceleration (dashed lines). The HPS (the solid black line) at 122 au with $h_1 = -1.35$ in Equation (4) is used. All other features are as defined in Figure 1.

energy for each of the spectra presented in Figure 1. In the first region, at $E \lesssim 0.1$ GeV, the HPS and its corresponding modulated TS spectrum have the same spectral indices for both of the considered values of h_1, because the modulation at these energies is such that the form of the HPS is retained. Up to ~0.6 GeV, modulation hardens the TS spectra significantly so that their spectral indices increase, while the unmodulated HPS gradually transitions to smaller indices. In the third region, above 1 GeV, the values of the spectral indices decrease as the forms of the modulated TS spectra and the HPS begin to converge. The spectral indices across nearly the entire considered energy range are larger than the DSA-associated index of -3 for $s = 2.5$. This is consistent with the condition of Equation (9). Even if a stronger TS with a compression ratio of $s = 3$ was considered, DSA would only be able to increase spectral indices smaller than -2.5 (see Equation (6)), which still confines spectral hardening to energies above ~3 GeV. At such high energies, however, the diffusion length scales of electrons become too large for DSA to be efficient. The left-hand panel of Figure 2 shows that the spectral indices of accelerated TS spectra do not exceed those of their corresponding spectra without acceleration at any energy. The spectra incident at the TS are shifted to higher energies though, which is why their spectral indices in Figure 2 are shifted to the right when acceleration is included. This illustrates the effect described by Equation (10).

The aforementioned shift to higher energies is also accompanied by an intensity increase. Indeed, the accelerated TS spectra in Figure 1 have consistently larger intensities than those without acceleration and by different amounts in each of the characteristically distinct energy regions. These acceleration-induced increases are accentuated in the right-hand side of Figure 2, where the ratios of electron intensities at the TS with re-acceleration effects to those without are plotted as a function of kinetic energy. These ratios may hereafter also be referred to as "re-accelerated factors" or "re-accelerated contributions to intensities." In the low-energy region, the indices $h_1 = -1.55$ and -1.35, which the TS spectra retain from the HPS, are shown in the right-hand panel of Figure 2 to correspond to re-accelerated factors of 3 and 2.6 respectively. Basically, the uncertainty in the value of the spectral index reported by Stone et al. (2013) for the HPS implies in turn an uncertainty in the magnitude of acceleration effects at the corresponding energies. Important to note is that the softer spectrum (with $h_1 = -1.55$) yielded the greater acceleration-induced intensity increase. In the transition region, where spectral indices become very large, the re-accelerated factors become smaller, with the smallest factor of ~1.5 attained around the same energies (0.4–0.6 GeV) where spectral indices peak. Continuing this trend, the re-accelerated contribution recovers to a factor of 1.7 above 1 GeV, where spectral indices become very small, before tapering off completely toward higher energies as the electrons' diffusion length scales become very large. When comparing the left- and right-hand sides of Figure 2 in this manner, a clear inverse correlation is observed between the spectral indices of distributions incident at the TS and the amounts by which their intensities are increased as a result of re-acceleration.

4.2. The Effects of Drifts on Electron Re-acceleration

The Sun alternates its magnetic polarity every 11 years. During the $A > 0$ cycle, the magnetic field lines emanate from the northern hemisphere of the Sun, and during the $A < 0$ cycle they emanate from the south. In response, electrons drift inward mainly along the HCS and poleward during the $A > 0$ cycle, while these patterns reverse during the $A < 0$ cycle. See also the review by Potgieter (2014a).

The effects of these drifts on electron spectra at the location of *Voyager* 1's crossing of the TS are illustrated in Figure 3 for both magnetic polarities. These TS spectra still display the three distinct regions similar to those in Figure 1, but with the transition region affected differently than before. The range of energies where drift effects become important for electrons (see also Nndanganeni & Potgieter 2016) overlaps with the energy region where the low-energy power law of the TS spectra begins to harden. Compared to the non-drift solutions of Figure 1, this power law is turned upward more rapidly in the TS spectra of Figure 3 and at lower energies, consequently increasing intensities in this transition region. This in turn implies larger hardening of the TS spectra: The left-hand side of Figure 4 shows that spectral indices go up to 1.4 as opposed to ~0.7 for the non-drift solutions in Figure 2. As a result, the drift solutions yield smaller re-accelerated factors in this region, attaining minimum values of ~1.25 as illustrated in the right-hand side of Figure 4. Evidently, neglecting drifts may lead to overestimations of the magnitude of acceleration effects depending on how TS spectra are modified and at which

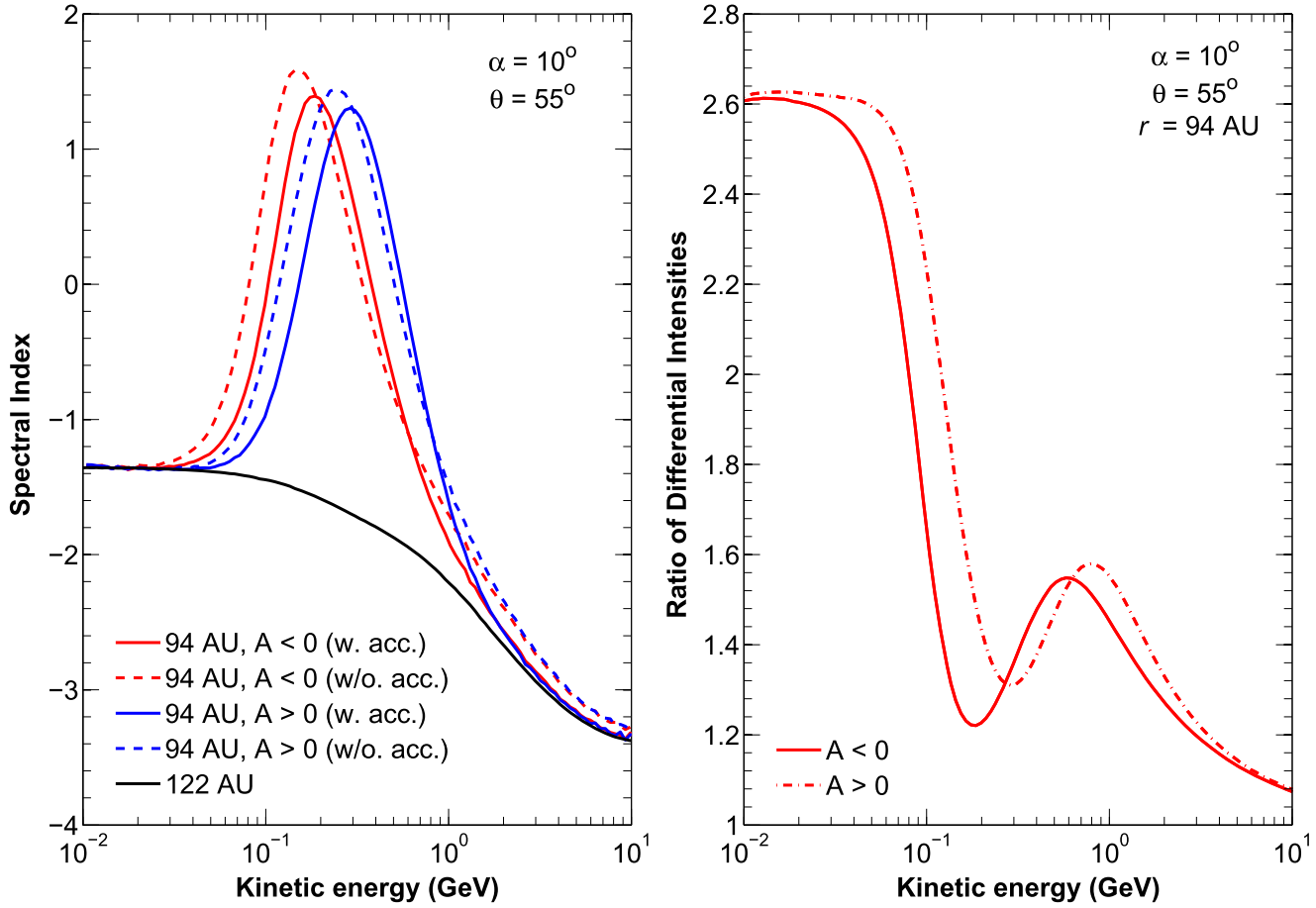

Figure 4. Left: the spectral indices of the energy spectra presented in Figure 3 with the lines representing the same configurations as defined in that figure. Right: ratios of the TS spectra presented in Figure 3 with acceleration to those without, indicative of what factor re-acceleration is contributing to intensities. The solid and dashed–dotted lines, respectively, represent the aforementioned ratios for the $A < 0$ and $A > 0$ cycles.

heliographic latitudes they are considered. The features caused by re-acceleration as reported in Figures 3 and 4 otherwise remain largely similar to those discussed in Section 4.1.

It follows from Figure 3 that the intensity levels of the re-accelerated TS spectra are raised by slightly smaller amounts during the $A < 0$ cycle than during the $A > 0$ cycle. This leads to polarity-dependent differences in the features of electron re-acceleration. The left-hand side of Figure 4 shows that spectral indices are somewhat larger for $A < 0$ than for $A > 0$, depending on the kinetic energy, which corresponds to generally smaller re-accelerated factors during the $A < 0$ cycle. The right-hand panel of Figure 4 shows how DSA raises intensities for $A > 0$ by larger amounts than for $A < 0$ up to ∼0.3 GeV and then again from ∼0.6 GeV. The polarity-dependent features of re-acceleration also appear to follow the inverse correlation between spectral hardness and the magnitude of acceleration effects. This interplay of processes is illustrative of the intricacies that need to be accounted for when studying CR acceleration within the context of their global transport and modulation; see also the discussion by Nndanganeni & Potgieter (2016).

5. Spatial Distributions of Re-accelerated Electrons

It remains to be discussed how electrons are distributed spatially after being re-accelerated at the TS and what contribution they make to overall intensities in different regions of the heliosphere. Their distribution throughout the heliosphere depends of course on the spatial dependences of modulation processes. To illustrate this, radial intensity profiles along a simulated *Voyager* 1 trajectory are presented in Figure 5 at a selection of energies for the two polarity cycles, and with and without re-acceleration at the TS. A notable feature of these profiles is the large intensity gradients in the heliosheath for the lower-energy electrons. The modulation of higher-energy electrons in the heliosheath is tempered by their larger diffusion length scales. The 200 and 1000 MeV electrons also experience larger drifts than at lower energies, where the modulation process is diffusion-dominated as shown in Figure 3, and hence their radial profiles show greater differences between the two polarities. Note that the 200 MeV intensities, especially, are higher in the outer heliosphere during the $A < 0$ polarity cycle than during the $A > 0$ cycle.

The ratios of these intensity profiles with acceleration to those without are presented in Figure 6. These ratios show that re-acceleration is indeed largest for the lower-energy electrons, with the re-accelerated factor for 16 MeV electrons peaking at a value of 2.6. While this intensity increase at the TS is significant, the assumed higher turbulence levels downstream of the TS do not allow re-accelerated electrons to be transported far into the heliosheath. Their contribution is easily overlooked relative to the steep increase of galactic electron intensities as they necessarily approach the values of the HPS.

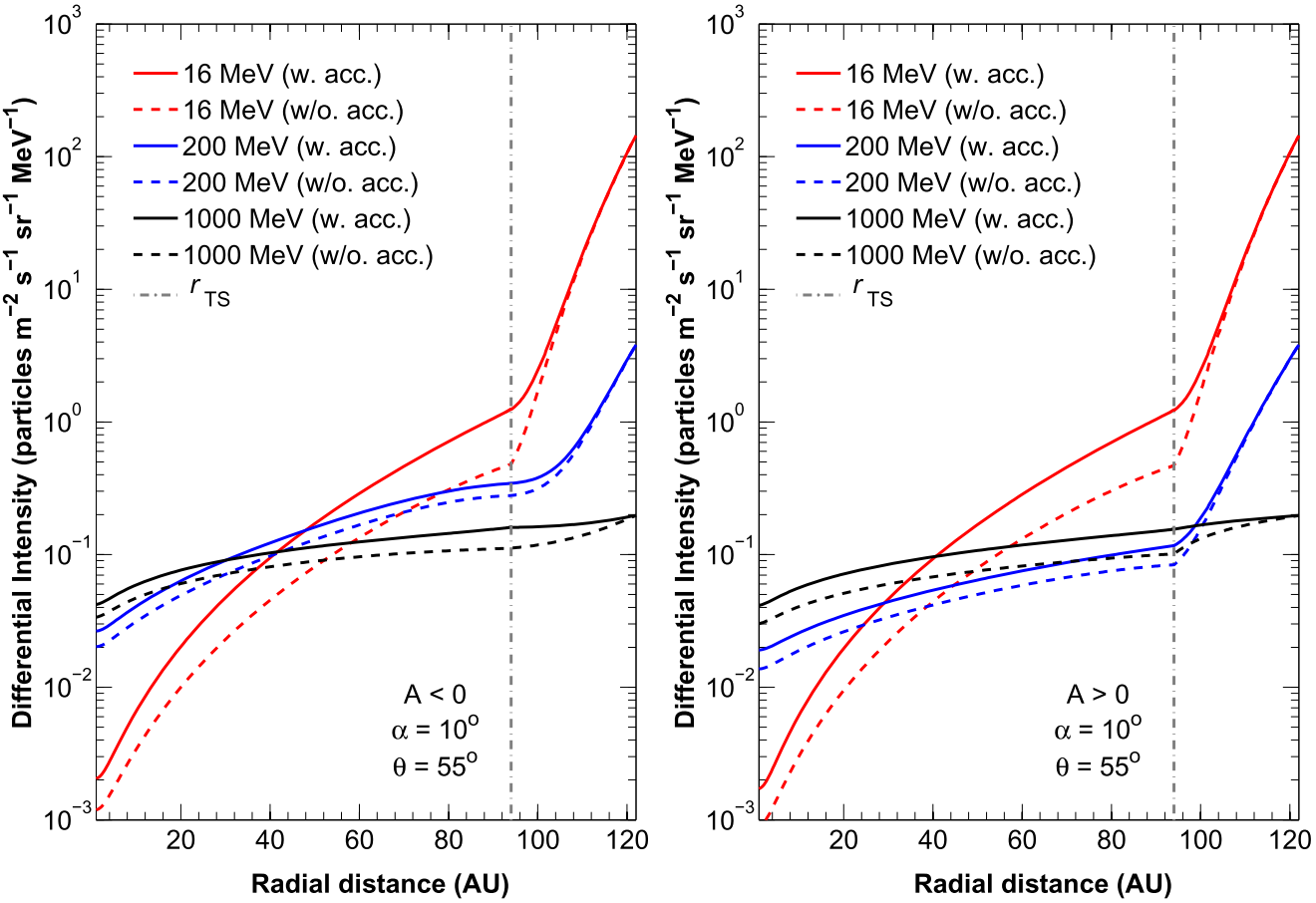

Figure 5. Radial intensity profiles for electrons at the energies as indicated in the legend for $A < 0$ (left panel) and $A > 0$ (right panel). Solid lines represent profiles with acceleration and dashed lines represent profiles without acceleration at the TS, which is positioned at $r_{TS} = 94$ au (the vertical dashed–dotted line). As before, the HPS with $h_1 = -1.35$ in Equation (4) is applied at 122 au. Profiles are shown for a polar angle (colatitude) of $\theta = 55°$ and $\alpha = 10°$.

Upstream of the TS, the transport of re-accelerated electrons is facilitated by larger diffusion coefficients. The model predicts that the contribution of re-accelerated 16 MeV electrons may double intensities of galactic electrons in the inner heliosphere. Their intensity at Earth is increased by a factor of 1.7–1.9, depending on the magnetic polarity. Unfortunately, this type of contribution will be mostly concealed in observations by Jovian electrons up to $\sim$ 30 MeV (Fichtner et al. 2000; Ferreira et al. 2001, 2004; Potgieter & Nndanganeni 2013).

It is interesting to note that drift-affected high-energy electrons, as displayed by the intensity ratios in Figure 6, show re-accelerated contributions in the inner heliosphere that are relatively large compared to those at the TS, for example, as depicted at 200 MeV. To understand this, it has to be borne in mind that the profiles of Figures 5 and 6 are presented along a single heliographical latitude. Processes such as polar perpendicular diffusion and drifts can transport these re-accelerated electrons across latitudes so that their relative contribution is altered from the outer to the inner heliosphere. Also note that drifts during the $A < 0$ cycle increase the re-accelerated contribution to electron intensities in the heliosheath, while the contribution in the inner heliosphere is relatively larger during the $A > 0$ cycle. At the TS, Figure 6 shows larger ratios for the $A > 0$ cycle than for the $A < 0$ cycle, which results from the softer spectral features during the former cycle as discussed in Section 4.2.

6. Discussion and Conclusions

The features of DSA, when applied to the re-acceleration of galactic electrons at the TS, is in many ways easy to overlook. Given the spectral features that electron spectra display in the outer heliosphere between 10 MeV and 10 GeV, spectral hardening cannot generally be expected to occur at these energies as a result of DSA at the TS. Instead, our modeling shows that DSA shifts spectra at the TS to higher energies, thereby only changing their slopes where the spectral index is not constant in terms of energy. DSA also raises the intensities of spectra at the TS by an amount that is inversely proportional to the value of their spectral indices. Given that CR detectors have no way of discerning whether an observed electron had been re-accelerated or not, these effects will not be easily recognized in observations. It is by virtue of events such as the intensity enhancements observed by the *Voyager* spacecraft prior to the TS crossings (e.g., McDonald et al. 2003) that the potential presence of DSA effects may be discovered.

The modeled intensity increases at the TS resulting from electron re-acceleration are of special interest at low energies. The model predicts that the re-acceleration of low-energy electrons increases their intensities by factors that are comparable to the magnitudes of the 6–14 MeV electron intensity enhancements reported by McDonald et al. (2003) and Stone et al. (2005, 2008). The proposition was made at the time of these enhancements' detection that they are indicative of re-

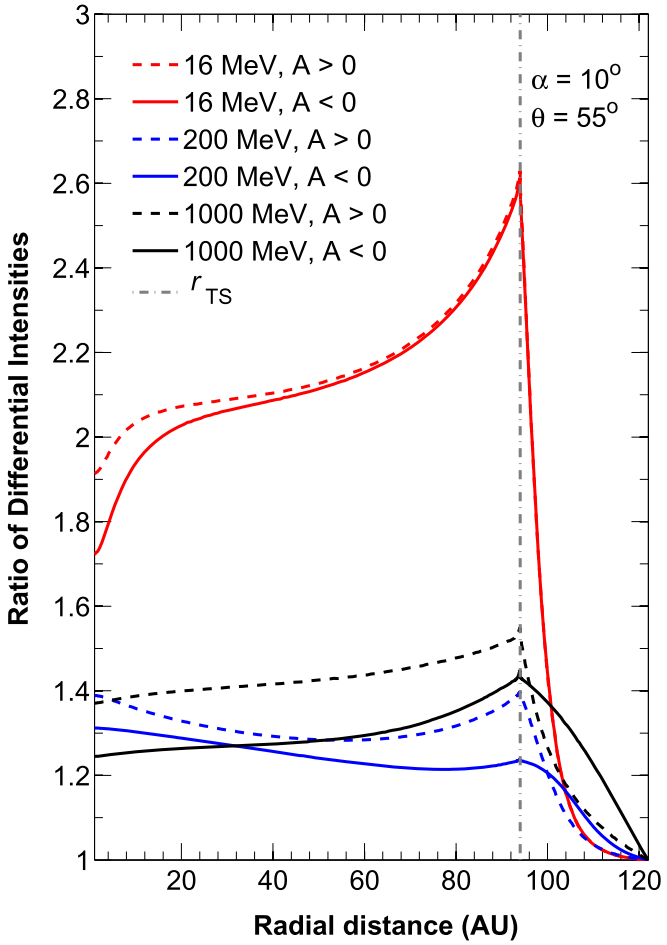

Figure 6. Ratios of the radial profiles of Figure 5 with acceleration to those without, shown for the $A > 0$ polarity cycle (dashed lines) and the $A < 0$ cycle (solid lines). The colors represent the same energies as in Figure 5.

acceleration at the TS, probably by way of DSA. For the case of electrons, the modeling results presented here support this proposition. The relatively short-lived and anisotropic nature of the enhancements may then be explained by invoking a mechanism such as that proposed by Giacalone & Jokipii (2006). This mechanism, simply explained, entails that re-accelerated electrons can be transported from different positions along the TS to the spacecraft during good magnetic connections, which may change significantly with time and position.

Although the modeling presented here illustrates the case for the involvement of DSA, alternative re-acceleration mechanisms must necessarily be considered in future work, such as stochastic acceleration and adiabatic heating in the heliosheath (e.g., Strauss et al. 2010), magnetic reconnection (Zank et al. 2014; le Roux et al. 2015), or a combination of different processes with DSA (Zank et al. 2015; le Roux et al. 2016).

Drifts are found to play an influential role in the re-acceleration process at higher energies, affecting both the magnitude of DSA-associated increases at the TS (by modifying incident energy spectra) and the transport of re-accelerated electrons throughout the heliosphere. Drifts can facilitate the transport of re-accelerated electrons up- or downstream of the TS during the two polarity cycles. *Voyager* 1, for instance, crossed the TS into the heliosheath in an $A < 0$ cycle. The transport of re-accelerated electrons into the heliosheath would thus have been enhanced by drifts at the time. See also Webber et al. (2008). At lower energies, re-accelerated electrons can make an appreciable contribution to the intensities of galactic electrons at the Earth, though Jovian electrons dominate their intensities in the inner heliosphere up to ~30 MeV. In the heliosheath, however, their contribution diminishes within 10 au from the TS. It therefore seems unlikely that the re-acceleration of these low-energy electrons by DSA would make any contribution to intensities in the very local interstellar medium.

As an avenue for future research, the implementation of a full 3D representation of the heliosphere will allow re-acceleration to be studied in different regions, such as at the heliospheric flanks and in the tail region. This will be explored with CR transport modeled using stochastic differential equations, following, e.g., Luo et al. (2013, 2016).

The features of electron re-acceleration presented here are of course subject to changes depending on the transport coefficients assumed. The magnitude of re-acceleration effects are especially sensitive, since modulating processes exist that can alter the form of spectra at the TS. The effects of such changes can nevertheless be easily anticipated bearing the inverse relationship between spectral hardness and DSA-associated intensity increases in mind. This also demonstrates the advantage of studying CR re-acceleration within the context of a comprehensive transport model. Indeed, for a physically representative transport configuration, the model reaffirmed and illustrated the global prevalence and manifestation of the effects of DSA in the heliosphere.

M.S.P. expresses his gratitude for the partial funding granted by the South African National Research Foundation (NRF) under the Incentive and Competitive Grants for Rated Researchers. R.D.S. thanks the NRF for financial support. P.L.P. thanks the NRF and the South African National Space Agency (SANSA) for partial financial support during his postgraduate study.

References

Adriani, O., Barbarino, G. C., Bazilevskaya, G. A., et al. 2015, ApJ, 810, 142
Axford, W. I. 1981, Proc. ICRC, 12, 155
Axford, W. I., Leer, E., & Skadron, G. 1977, Proc. ICRC, 11, 132
Bisschoff, D., & Potgieter, M. S. 2014, ApJ, 794, 166
Burger, R. A., Potgieter, M. S., & Heber, B. 2000, JGR, 105, 27447
Burlaga, L. F., Ness, N. F., Acuña, M. H., et al. 2005, Sci, 309, 2027
Burlaga, L. F., Ness, N. F., Acuña, M. H., et al. 2008, Natur, 454, 75
Caballero-Lopez, R. A., Moraal, H., & McDonald, F. B. 2010, ApJ, 725, 121
Cummings, A. C., Stone, E. C., Heikkila, B. C., et al. 2016, ApJ, 831, 18
Decker, R. B., Krimigis, S. M., Roelof, E. C., et al. 2005, Sci, 309, 2020
Engelbrecht, N. E., & Burger, R. A. 2015, AdSpR, 55, 370
Ferreira, S. E. S., & Potgieter, M. S. 2002, JGR, 107, 1221
Ferreira, S. E. S., Potgieter, M. S., & Burger, R. A. 1999, Proc. ICRC, 7, 77
Ferreira, S. E. S., Potgieter, M. S., Burger, R. A., et al. 2001, JGR, 106, 29313
Ferreira, S. E. S., Potgieter, M. S., Burger, R. A., & Heber, B. 2000, JGR, 105, 18305
Ferreira, S. E. S., Potgieter, M. S., & Webber, W. R. 2004, AdSpR, 34, 126
Ferreira, S. E. S., & Scherer, K. 2004, ApJ, 616, 1215
Fichtner, H., Potgieter, M. S., Ferreira, S. E. S., & Burger, R. A. 2000, GeoRL, 27, 1611
Fisk, L. A., Gloeckler, G., & Zurbuchen, T. H. 2006, ApJ, 644, 631
Fisk, L. A., Kozlovsky, B., & Ramaty, R. 1974, ApJL, 190, L35
Giacalone, J., Drake, J. F., & Jokipii, J. R. 2012, SSRv, 173, 283
Giacalone, J., & Jokipii, J. R. 2006, ApJL, 649, L137
Gurnett, D. A., Kurth, W. S., Burlaga, L. F., & Ness, N. F. 2013, Sci, 341, 1489
Heber, B., & Potgieter, M. S. 2006, SSRv, 127, 117
Jokipii, J. R. 1982, ApJ, 255, 716

Jokipii, J. R. 1986, JGR, 91, 2929
Jokipii, J. R. 1987, ApJ, 313, 842
Jokipii, J. R., Giacalone, J., & Kóta, J. 2007, P&SS, 55, 2267
Jokipii, J. R., & Kóta, J. 1989, GeoRL, 16, 1
Jones, F. C., & Ellison, D. C. 1991, SSRv, 58, 259
Langner, U. W., & Potgieter, M. S. 2005, AdSpR, 35, 2084
Langner, U. W., Potgieter, M. S., Fichtner, H., & Borrmann, T. 2006a, ApJ, 640, 1119
Langner, U. W., Potgieter, M. S., Fichtner, H., & Borrmann, T. 2006b, JGR, 111, A10106
Langner, U. W., Potgieter, M. S., & Webber, W. R. 2004, AdSpR, 34, 138
le Roux, J. A., Potgieter, M. S., & Ptuskin, V. S. 1996, JGR, 101, 4791
le Roux, J. A., Zank, G. P., Webb, G. M., & Khabarova, O. 2015, ApJ, 801, 112
le Roux, J. A., Zank, G. P., Webb, G. M., & Khabarova, O. V. 2016, ApJ, 827, 47
Lee, M. A., Fahr, H. J., Kucharek, H., et al. 2009, SSRv, 146, 275
Luo, X., Potgieter, M. S., Zhang, M., et al. 2016, ApJ, 826, 182
Luo, X., Zhang, M., Rassoul, H. K., Pogorelov, N. V., & Heerikhuisen, J. 2013, ApJ, 764, 85
McDonald, F. B., Stone, E. C., Cummings, A. C., et al. 2003, Natur, 426, 48
Menn, W., Adriani, O., Barbarino, G. C., et al. 2013, AdSpR, 51, 209
Moeketsi, D. M., Potgieter, M. S., Ferreira, S. E. S., et al. 2005, AdSpR, 35, 597
Ngobeni, M. D., & Potgieter, M. S. 2015, AdSpR, 56, 1525
Nndanganeni, R. R., & Potgieter, M. S. 2016, AdSpR, 58, 453
Parker, E. N. 1958, ApJ, 128, 664
Parker, E. N. 1965, P&SS, 13, 9
Pesses, M. E., Eichler, D., & Jokipii, J. R. 1981, ApJL, 246, L85
Potgieter, M. S. 1996, JGR, 101, 24411
Potgieter, M. S. 2014a, AdSpR, 53, 1415
Potgieter, M. S. 2014b, BrJPh, 44, 581
Potgieter, M. S., & Moraal, H. 1985, ApJ, 294, 425
Potgieter, M. S., & Moraal, H. 1988, ApJ, 330, 445
Potgieter, M. S., & Nndanganeni, R. R. 2013, Ap&SS, 345, 33
Potgieter, M. S., Vos, E. E., Munini, R., et al. 2014, SoPh, 289, 391
Potgieter, M. S., Vos, E. E., Munini, R., Boezio, M., & Di Felice, V. 2015, ApJ, 810, 141
Richardson, J. D., Kasper, J. C., Wang, C., Belcher, J. W., & Lazarus, A. J. 2008, Natur, 454, 63
Schwadron, N. A., Lee, M. A., & McComas, D. J. 2008, ApJ, 675, 1584
Steenberg, C. D., & Moraal, H. 1999, JGR, 104, 24879
Stone, E. C., Cummings, A. C., McDonald, F. B., et al. 2005, Sci, 309, 2017
Stone, E. C., Cummings, A. C., McDonald, F. B., et al. 2008, Natur, 454, 71
Stone, E. C., Cummings, A. C., McDonald, F. B., et al. 2013, Sci, 341, 150
Strauss, R. D., & Potgieter, M. S. 2014, AdSpR, 53, 1015
Strauss, R. D., Potgieter, M. S., Ferreira, S. E. S., Fichtner, H., & Scherer, K. 2013, ApJL, 765, L18
Strauss, R. D., Potgieter, M. S., Ferreira, S. E. S., & Hill, M. E. 2010, A&A, 522, A35
Teufel, A., & Schlickeiser, R. 2003, A&A, 397, 15
Webber, W. R., & McDonald, F. B. 2013, GeoRL, 40, 1665
Webber, W. R., McDonald, F. B., Cummings, A. C., et al. 2008, JGR, 113, A10108
Webber, W. R., McDonald, F. B., Cummings, A. C., et al. 2012, GeoRL, 39, 6107
Zank, G. P., Hunana, P., Mostafavi, P., et al. 2015, ApJ, 814, 137
Zank, G. P., le Roux, J. A., Webb, G. M., Dosch, A., & Khabarova, O. 2014, ApJ, 797, 28